Unveiling the Full Dynamical and Reactivity Profiles of Acetylcholinesterase: A Comprehensive All-Atom Investigation

Frédéric Célerse,[†,‡,¶] Louis Lagardère,[†,§] Yasmine Bouchibti,[‡] Florian Nachon,[‖] Laurent Verdier,[⊥] Jean–Philip Piquemal,[†] and Etienne Derat[*,‡]

†*Sorbonne Université, LCT, UMR 7616 CNRS, 75005, Paris, France*

‡*Sorbonne Université, IPCM, UMR 8232 CNRS, 75005, Paris, France*

¶*current adress: LCMD EPFL, CH–1015 Lausanne, Switzerland*

§*Sorbonne Université, IP2CT, FR 2622 CNRS, 75005, Paris, France*

‖*Département de Toxicologie et Risques Chimiques, IRBA, 91223, Brétigny-sur-Orge, France*

⊥*Centre d'Etudes du Bouchet, 91740, Vert-le-Petit, France*

E-mail: etienne.derat@sorbonne-universite.fr

Abstract

Acetylcholinesterase is one of the most significant known serine hydrolases, governing the mammalian nervous system. Its high rate speed, operating at the diffusion limit, combined with its buried active site feature, has made it a subject of extensive research over the last decades. Despite several studies focused on atomistic details of its different steps, a comprehensive theoretical investigation of the entire catalytic cycle has not yet been reported. In this work, we present an intuitive workflow aiming at describing the full dynamical and reactive profiles of AChE by coupling extensive Steered Molecular Dynamics (SMD) simulations for ligand diffusion and hybrid Quantum Mechanics/Molecular Mechanics (QM/MM) computations to decipher the complete reactivity of the substrate within the enzyme. This comprehensive approach provides a broader view of the interconnections between each step that would not be readily accessible if studied independently. Our simulations reveal that although individual steps do not indicate any strong limiting step, a solvent water molecule reorganization between the acylation and deacylation processes through the reactivity results in an energy cost of 20 kcal/mol. The observed barrier surpasses all others and discloses insights on a strong polarization effect acting on water molecules near the active site. An AMOEBA polarizable Molecular Dynamics simulation tends to confirm this assumption by capturing a substantial dipole moment (3.10 D) on the water molecule closest to the reaction site. These results shed light on the crucial correlation between this high–energy water reorganization and the polarization of confined water molecules. Consequently, carefully considering and modeling buried (polarizable) water molecules is of paramount importance when modeling full enzymatic activity. Therefore, this work will also provide valuable insights for future research on related enzymes with buried active sites.

Keywords

Acetylcholinesterase; biocatalysis; enzymology; molecular dynamics; QM/MM

Introduction

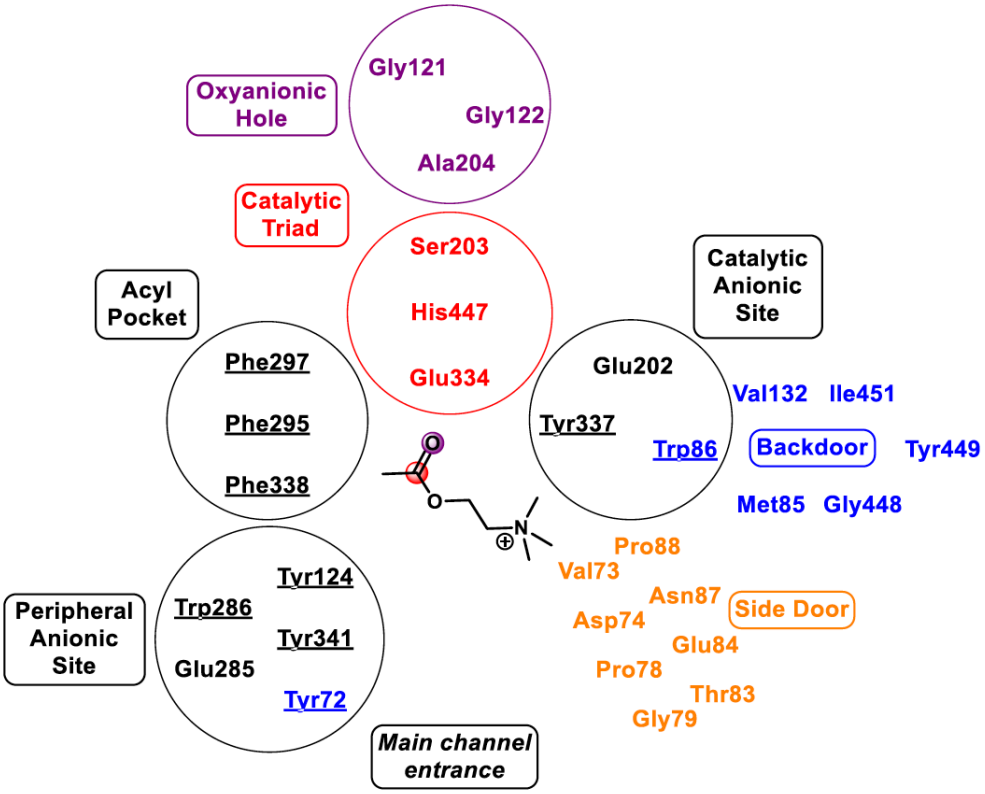

Figure 1: Schematic view of the active site, main channel and possible exit ways (backdoor and side door) of acetylcholinesterase, highlighting their key components.

Binding and unbinding of ligands within enzymatic systems play a pivotal role in understanding protein activity and designing more potent drugs.[1–3] For decades, numerous studies have made significant efforts to decipher the intrinsic correlation between the protein–ligand interaction strength within the enzyme's active site and the binding affinity, resulting in interpretations of its drug efficacy.[4–8] While isolating the main interactions between ligands and active sites is common, it becomes tedious when other subtle interactions could interfere in the binding/unbinding process.

One relevant example is when dealing with enzymatic active sites buried within the enzyme structure, a common occurrence in enzymatic catalysis.[9,10] These buried active sites offer protection to reactive species, such as strong oxidants or specific protonation states,

from environmental conditions.[11] Due to their constrained nature, buried active sites exhibit enhanced selectivity through interactions with various residues in the active site.[11,12] Among the enzymes featuring buried active sites, acetylcholinesterase (AChE) stands out as one of the most intriguing examples, with its active site located deep within a narrow gorge (20 Å). This enzyme plays a crucial role in terminating nerve signal transmission at cholinergic synapses by hydrolyzing the neurotransmitter acetylcholine (ACh) into acetate and choline (Ch).[13,14] AChE is especially known for its remarkable catalytic speed, operating at a diffusion-regime speed,[15,16] which has earned it significant attention from researchers in the field of biology.[17–27] Fig 1 depicts a simplified schematic view of AChE's active site and main channel. The catalytic triad (in red) enables ACh cleavage, while the Catalytic Aromatic Site (CAS) and Acyl pocket stabilize ACh within the active site,[28–30] with the oxianion hole (in purple) constraining the ACh conformation through hydrogen bonding.[31,32] ACh and Ch can respectively enter and exit through the main channel, whereas a backdoor (in dark blue) appears as an alternative route for small–sized ligands when the main channel is obstructed.[33] Furthermore, a third exit pathway was identified across the AChE's Ω loop (in orange) and named as the side door. Thanks to the strong fluctuation resulting from the Ω loop,[34–36] and although its opening frequency is relatively low, it has been shown that this pathway enables the exit of very small ligands.[37–40] At the end of the gorge, connecting the outside and the active site, the Peripheral Aromatic Site (PAS) acts as a buffer between the CAS and the exit, guiding ligands through hydrogen bonding and cation-π interactions during their binding/unbinding process, respectively.[41–43]

Given the complexity arising from all the possible non–covalent interactions between ligands and several amino acids of AChE (particularly being part of the PAS, CAS, acyl pocket, and oxyanion hole), conducting a comprehensive study that links the contribution of each subunit to the dynamics and stability of each ligand represents a significant experimental challenge. Moreover, the need to incorporate different exit pathways in the conventional model further complicates the mechanistic scheme of this enzyme, making AChE an ex-

tremely tough system to properly investigate experimentally.

In this regard, molecular modeling has emerged as the method of choice for demistifying the key factors influencing these processes.[44–46] However, these events are substantially rare on the timescale of molecular dynamics (MD), typically spanning a few microseconds at best.[47] As a result, extensively sampling such rare events using conventional MD simulations is computationally impractical, leading to the use of enhanced sampling strategies.[48–50] Among the plethora of methods available in the literature, Steered Molecular Dynamics (SMD) can be seen as a fine–tuned tool for capturing the non–covalent interactions governing ligand diffusion.[51,52] SMD involves applying a harmonic potential to selected atoms, inducing their motion in specific directions. Both easy to use and intuitive, this enhanced sampling technique has already been used to study ligand binding and unbinding from enzymatic active sites by steering ligands out of buried active sites through the main channel.[53–56] Furthermore, when employed with suitable parameters, SMD has been shown to achieve accurate energetic predictions associated with binding/unbinding events.[57–59]

Afterwards, SMD has also been applied on AChE to design new drugs targeting various diseases that affect the human nervous system, such as Alzheimer's disease.[60] An optimal drug should indeed reversibly inhibit AChE by non–covalently blocking its buried active site access. Several atomistic–scale studies have explored the inhibition mechanisms on well–known drugs (e.g., Huperzine,[46] E2020,[61] Donepezil[60]) and correlated their dynamical behavior with their respective non–covalent interactions with AChE, such as cation-π and hydrogen bonding, and water molecules (water bridges).[43,46,60–62] Besides, the role of water molecules was carefully ascertain through several works. Henchman et al. thus demonstrated the presence of a water flux occuring through the main channel by using a 10–ns MD.[63] While water molecules within the active site are strongly structured and barely mobile, those present in the gorge are substantially more mobile, thus revealing the presence of a flow of water molecules that may assist in the diffusion of the ligand during the entry/exit process of any ligands through the main channel. This major role of water in ligand diffusion

has also been highlighted in various studies conducted by the team of Bandyopadhyay et al.[64–66] They demonstrated that the water model used in MD simulations significantly affects the dynamics of the ligand within the gorge. Taken together, these findings call for caution regarding the role of water molecules in the theoretical model related to AChE.

Despite the huge amount of individual studies covering various aspects of AChE, a comprehensive investigation encompassing its entire dynamics and reactivity as a single study remains to be conducted. In this work, drawing inspiration from existing studies on modeling the different catalytic steps of AChE, we present a comprehensive and intuitive pipeline to simulate the complete dynamical and reactivity profile of AChE. Our focus is on exploring the energetic contributions of each step in AChE's catalytic cycle, from ACh entrance to Ch and acetate exit, using a combination of QM/MM and SMD simulations. For each step, we carefully analyze the influence of various non–covalent interactions, such as hydrogen bonding patterns and cation–π interactions. Non-covalent interactions involving water molecules are also investigated using several physical tools. In particular, we stake out the fluctuation of the dipole moment of water molecules confined within the buried active site, in line with the findings of Henchman et al. regarding the presence of potent structured water molecules in this region.[63] Ultimately, the combination of our ensemble of simulations and interpretations enables us to provide a comprehensive AChE model and identify the rate–limiting step throughout this cycle. The intuitive nature of our model allows for its potential application to future studies involving other enzymes with buried active sites.

Computational details

Building initial AChE systems

The initial systems considered throughout this work are based on the crystallographic structure of the aged form of AChE after inhibition by the tabun nerve agent (PDB: 3DL7[67,68]). This structure was released by the group of Nachon et al. and was used as starting point,

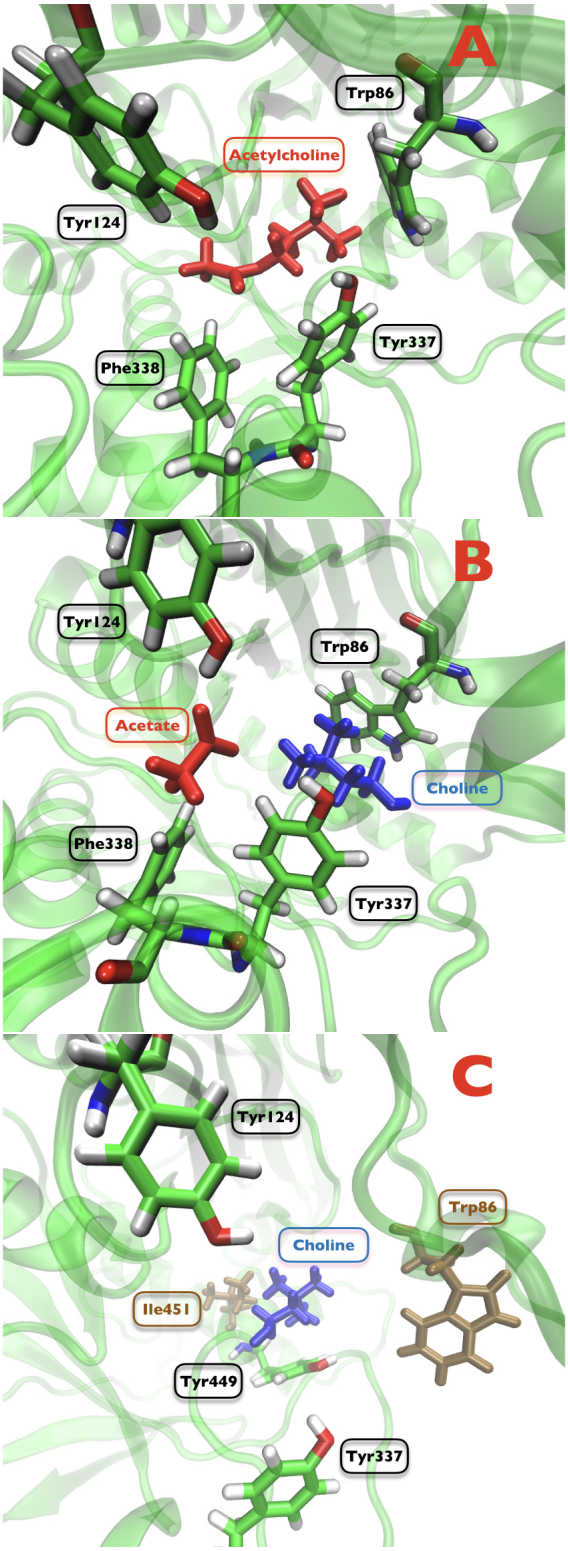

Figure 2: A) Screenshot of the acetylcholine substrate (in red) docked within the active site of AChE. Several aromatic residues contributing to the stabilization of acetylcholine in CAS and PAS are depicted B) Screenshot of the choline (in blue) and the acetate (in red) docked within the active site of AChE. Several aromatic residues contributing to the stabilization of acetylcholine in CAS and PAS are depicted C) Screenshot of the choline (in blue) docked within the active site of AChE and in front of the backdoor. Several aromatic residues contributing to the stabilization of acetylcholine in CAS and PAS are depicted and residues in brown were used to calibrate the SMD vector (see next subpart). All the structures were obtained after equilibration and was considered as our starting point for SMD simulations.

as previous works by our group are based on it.[26,27] To study the motion of ACh and Ch through the main channel and backdoor of AChE, we consecutively built 3 different systems: the first containing AChE before the cleavage reaction (system A in Fig 2A) and the others containing Ch and acetate just after the cleavage reaction (system B in Fig 2B) and Ch located near the backdoor (system C in Fig 2C).

We only considered the AChE's monomer form (chain A), and glycols (PG4 and P6G) and glucosamine (NAG) were deleted from the initial structure. The covalently linked phosphorus group to the serine residue belonging to the catalytic triad (labeled as Ser203 hereinafter) was also removed. Standard protonation states were taken into account for all residues except Glu202, which was protonated due to its demonstrated increased basicity compared to usual glutamic acid.[27]

The initial structures of ACh, Ch, and acetate were built using Gaussview software[69] and manually docked at the active site of their respective structures using VMD software.[70] Subsequently, these structures were placed in a cubic water box of dimensions 100 Å x 100 Å x 100 Å, and the structural water molecules were conserved to ensure that no physical unfolding of the secondary structures occurred. The total charge of the systems was then neutralized using 8 chloride ions. In the end, we obtained 2 distinct systems, labeled as AChE+ACh and AChE+Ch, with respectively 94,506 atoms and 94,509 atoms, where 8,288 atoms belong to the AChE enzymatic structure.

All simulations were performed using NAMD 2.9 software in the NPT canonical ensemble.[71] The additive non–polarizable force field CHARMM22/CMAP was employed, with a rigid TIP3P model for water molecules.[72–74] Valence, charges, and Van der Waals parameters for ACh, Ch, and acetate were taken from the CHARMM36 library for small molecules.[75] The Beeman–Brünger–Karplus (BBK) integrator was used for solving the Newton equations with an integration timestep of 2 fs. The temperature was kept fixed at 300 K using a Langevin thermostat with a damping coefficient of 1 ps^{-1}, and the pressure was maintained at 1 bar using a Langevin piston with a period of 100 steps and a decay of 50 steps.[76]

Periodic Boundary Conditions (PBC) were applied using the Particle Mesh Ewald (PME) methodology[77] with a grid size of 120 Å x 120 Å x 120 Å and a spacing of 1 Å, and an Ewald cutoff of 7 Å was used without switching functions.

Each system were first minimized for 10,000 steps, followed by a gradual heating to 300 K over 5 ns. The root mean square deviation (RMSD) of all atoms (proteins and water molecules) was used to ensure the proper equilibration of each prepared system. The structures corresponding to systems A and B (Fig 2A and B) were extracted from the AChE+ACh and AChE+Ch simulations respectively, while the structures corresponding to system C (Fig 2C) were obtained from an additional 50 ns simulation of the AChE+Ch system. The selection of structures was carried out manually, ensuring that the choline was positioned close to the backdoor.

Steered Molecular Dynamics

The SMD methodology was used to induce the departure of each ligand from the active site within a few nanoseconds of simulation. The same initial MD parameters used during the equilibration process were applied. The set of initial structures from systems A, B and C, obtained previously, served as our starting points for the SMD simulations.

An external SMD potential was applied to the Center of Mass (COM) of each substrate (ACh and Ch). The SMD vectors were evaluated before starting any SMD simulations. We employed two different SMD vectors: one vector corresponding to the distance coordinates between the center of mass (COM) of the substrate and the COM of the backbone of three different residues located at the entrance of the channel (Leu76, Trp286, and Glu292), and the other SMD vector with coordinates between the COM of Ch and the COM of the backbone of two different residues localized at the entrance of the backdoor (Trp86 and Ile451). The first vector was used for the SMD simulations involving ligand entering/exiting through the main channel (e.g., systems A and B), and the second vector was used when ligands crossed the backdoor (e.g., system C). The backbone carbons of the first and last residue and the

oxygen of Ser203 were kept fixed during all simulations to prevent fictive motions of the AChE enzyme during the pulling process. A spring constant of 4.00 kcal/(mol.Å^2) and an SMD velocity of 0.005 Å/ps were used. These setups correspond to the best sets used in the literature for such AChE SMD studies.[61]

However, to ensure the consistency of these setups, a test system with an AChE inhibited non–covalently by Huperzine–A (HUPA) was benchmarked. Parameters used for HUPA are provided in Section 1 of Supplementary Informations (SI), and the same conditions as explained previously were applied to prepare the AChE+HUPA system. HUPA was steered in the same conditions (direction and speed) as ACh through the main channel (e.g., system A), ensuring consistency with our future simulations.

For each system (systems A,B,C + AChE+HUPA), thirty independent simulations of 5 ns were performed, resulting in a total of 150 ns/system. The pulling works were calculated for each trajectory, and the Potential of Mean Force (PMF) was reconstructed along the pulling direction (considered here as our reaction coordinate) using the Jarzynski equality.[78,79]

QM/MM setup

In addition to studying the diffusion of ACh/Ch, a comprehensive understanding of the dynamical and reactivity profile of AChE requires an insightful investigation of its two key reactions that involves AChE and ACh: acylation and deacylation. To simulate these steps, we resorted to QM/MM simulations. They were based on the same PDB files used for the SMD simulations. ACh was positioned at the active site, adopting orientations obtained from previously equilibrated molecular dynamics simulations, and it served as the starting point for SMD. An 8 Å layer of water molecules was created around AChE using Chimera 1.10.1.[80] The whole enzyme, excluding the catalytic triad, underwent full relaxation using the CHARMM software with CHARMM22 parameters.[81]

The protonation states of residues with acidic or basic side chains were determined using Propka.[82,83] Key reactive residues at the active site, including Glu202, were protonated

based on previously published results derived from QM/MM computations.[27] The QM zone comprised the catalytic triad, featuring the critical Ser203 residue (excluding the nitrogen of the peptide chain), the imidazole ring of His447, and the acetate of Glu334. The oxyanion hole, which includes Gly121, the carbonyl of Gly120, the amine and alpha carbon of Gly122, Ala204, and the amine and carbon of Gly205, was also part of the QM zone. Protonated Glu202 and ACh were included as well. The optimized MM zone encompassed all atoms from the QM zone, along with 19 water molecules and aromatic residues from the enzyme gorge. Additionally, residues (Glu202, Glu450, Ser229, and Tyr428) and two water molecules that formed a hydrogen bond network with Glu334 were present in the MM zone. The rest of the enzyme and the surrounding water molecules were included in MM but not optimized. The entire MM region, both optimized and not optimized, polarized the QM area through an electrostatic embedding scheme, including the charge shift correction.

Geometries were optimized using the HDLCOpt module in Chemshell 3.1b1.[84] The QM energetic data was computed using Turbomole V6.4[85] with the DFT functional B3LYP[86] and the dispersion correction D3.[87] The def2-SV(P) basis set was employed for all atoms.[88] MM data was generated by the DL_POLY_3 interface in Chemshell,[84,89,90] based on CHARMM22 parameters.[73,74] The scans were conducted using scripting tools in Chemshell. All stationary points and transition states were located via full-geometry optimization. Subsequently, two series of single points (SP) were performed: one with Turbomole at the B3LYP–D3 level with the def2–TZVPP basis set, and the second with ORCA[91] at the DLPNO–CCSD(T) level with the same def2–TZVPP basis set, to verify the accuracy of the DFT calculations. The energy obtained from the two sets of B3LYP–D3 computations was added to the MM energy provided by Chemshell to obtain the QM/MM energy for comparison purposes. Basis-)set convergence was estimated using the two sets of B3LYP–D3 calculations. The DLPNO–CCSD(T) method has demonstrated an accuracy of 1 kcal/mol (on the FH and S66 test sets) with the NormalPNO setting used in our work.[92]

Polarizable Molecular Dynamics

In addition to the SMD simulations and QM/MM computations, an MD simulation was conducted to evaluate the fluctuation of the dipole moment of water molecules confined within the active site of AChE. The simulation was carried out for system A (e.g., Fig 2A) using the GPU version of Tinker–HP.[93] All parameters for AChE, ions, and water molecules were converted from CHARMM to AMOEBA using the AMOEBABIO18 force field and the tools available in the Tinker 8 software.[94–97] However, since ACh parameters for AMOEBA were not available in the literature, we manually parametrized it following the standard procedure of Ren et al. (see section 2 in SI). Langevin molecular dynamics simulations were performed using the BAOAB–RESPA1 integrator with a 10 fs outer timestep,[98] a preconditioned gate gradient polarization solver (with a 10^{-5} convergence threshold), hydrogen–mass repartitioning (HMR), and random initial velocities. PBC were treated using the Smooth Particle Mesh Ewald (SPME) method with a grid of dimensions 128 Å x 128 Å x 128 Å . The Ewald cutoff was set to 7 Å and the Van der Waals cutoff to 9 Å.

The system was initially minimized until reaching an RMS of 1 kcal/mol, then slowly heated to 300K, and further equilibrated in the NVT and then NPT ensemble for a few nanoseconds. After equilibration, a 100 ns conventional MD simulation was performed, and snapshots were saved every 10 ps. For each frame, the dipole moments of the water molecules within the active site were computed using the analyze module available in the Tinker–HP software.[99]

Results and discussion

Validation against experimental results

First and foremost, to ensure the reliability of our SMD simulations throughout this study, we evaluated the accuracy of our SMD parameters by investigating the AChE+HUPA test

system. Experimentally, it has been determined that HUPA binds to AChE with a free energy difference of -9.2 kcal/mol at ambient temperature.[100] The resulting PMF from our 30 SMD trajectories is provided in Fig S1 in section 3 of SI and reveals a free energy difference of -11 kcal/mol between HUPA outside and inside the AChE CAS. With an error of 2 kcal/mol, we can estimate that our SMD parameters are enough robust and can be safely used for all the systems of interest in our next simulations.

Step 1: Entrance of acetylcholine

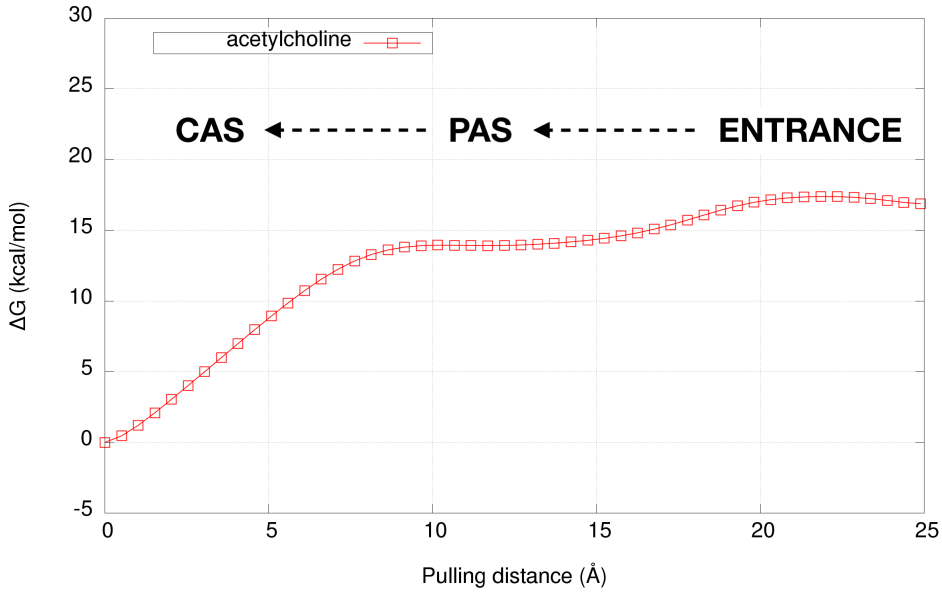

Figure 3: PMF describing the diffusion of acetylcholine into the AChE's gorge.

Studying the dynamical profile of AChE starts by assessing the ability of ACh to be docked into the CAS. Fig 3 displays the Potential of Mean Force (PMF) obtained from our 30 SMD simulations performed on system A (Fig 2A). Our results demonstrate that ACh is strongly stabilized within the CAS with a free energy difference of -17 kcal/mol. Additionally, a smooth stabilization is observed in the PAS, resulting in a binding energy of -3 kcal/mol between ACh and the PAS, followed by -14 kcal/mol to transfer ACh from the PAS to the CAS. Overall, these exothermic processes aligns with the well–known high affinity between AChE and its natural substrate.[101,102]

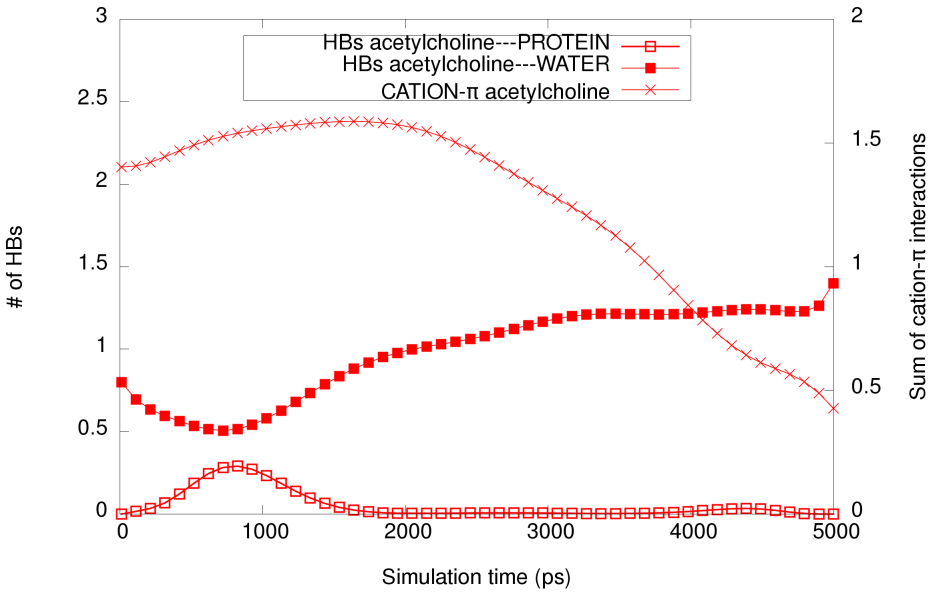

Figure 4: Non–covalent interactons between the protein, the ligand, and the water, depicted as a function of simulation time.

Our simulations show that ACh entry into the CAS is facilitated by several non–covalent interactions. Especially, cation-π interactions are observed between ACh's trimethylammonium moiety and several aromatic amino acids, while hydrogen–bonding occur between ACh's alcohol moiety and both AChE residues and water molecules within the gorge and the active site. Concerning the cation–π interactions, we ascertained to quantify their respective strengthness by resorting to an analysis tool released by Parrinello et al.[43] Additionally, we quantified the Hydrogen–bonding behavior between ACh, water solvent, and AChE. Fig 4 shows the results over simulation time, depicting strong cation–π and hydrogen–bonding interactions with AChE during entry. In particular, Tyr124, Tyr337, Phe338 and Tyr341 were identified as the most interacting residues during the binding of ACh (see Fig S2 in section 4 of SI).

Interestingly, as illustrated in Fig 4, we observed weak hydrogen bonding interactions between ACh and AChE, except when ACh was bound inside the CAS, concomitant with the loss of hydrogen bonding interactions with water molecules. This observation suggests that the desolvation/resolvation process of ACh during the entire dynamic process poses a

non-trivial challenge. Further analyses, presented in Figs S3 and S4 in SI, reveal a subtle correlation between the low occupancy of water molecules in the gorge and the extended accessible surface area of water molecules within the gorge, consistent with the conformational changes of the gorge during ACh dynamics. These observations imply a demanding resolvation process when ACh is exiting through the main channel, or more interestingly a a strong modification of the waters' network inside the CAS/PAS when ACh is bound.

Step 2: Hydrolysis of acetylcholine

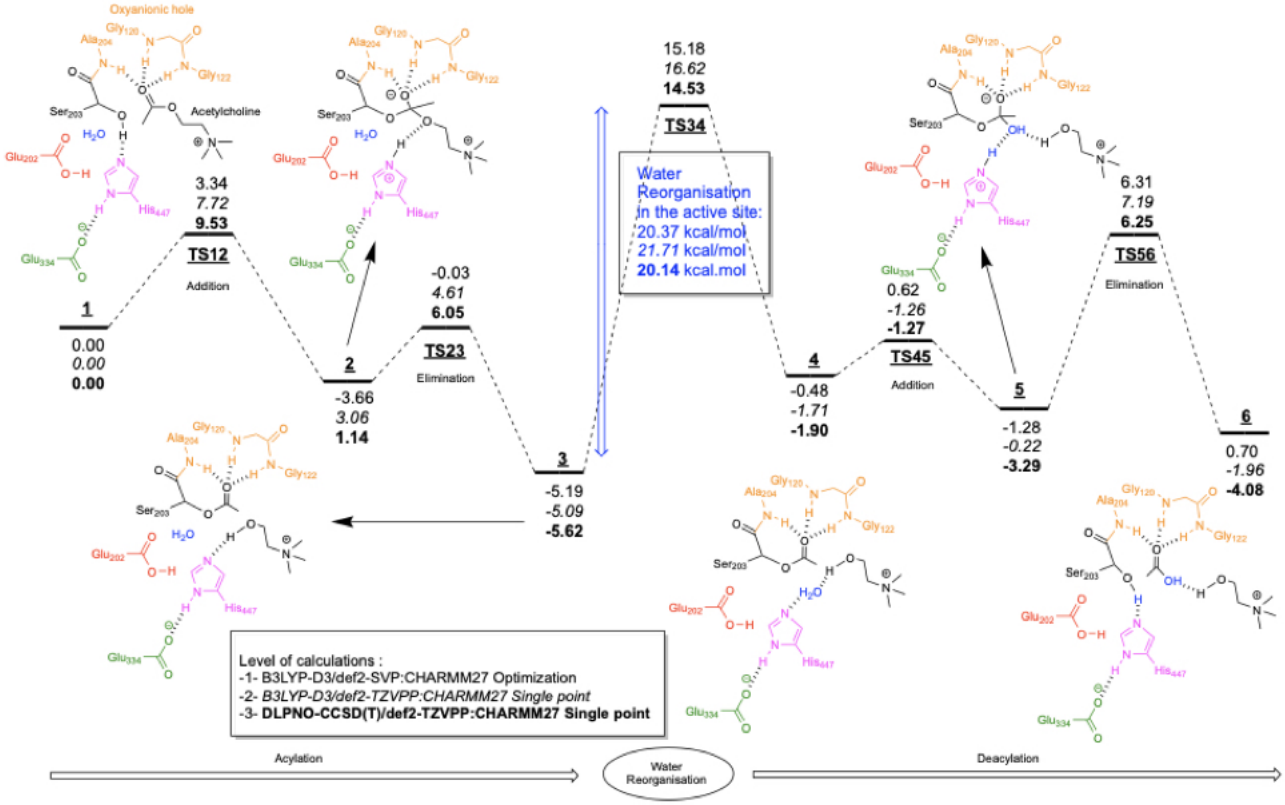

Figure 5: Reaction profile for the acylation and deacylation of acetylcholine in the active site of AChE, as computed by QM/MM simulations.

Now that the ACh's stability within the active site has been assessed, the next step is to investigate the hydrolysis of the substrate, which follows ACh's entrance (Step 1). Hydrolysis of ACh is commonly described in textbooks as a two–step process.[13,14] The first step involves the transfer of the acetyl moiety to Ser203, known as acylation, while simultaneously releasing Ch. The second step, called deacylation, involves the regeneration of a free Ser203. In our investigation, we resorted to QM/MM computations to study the complete mechanism, combining acylation and deacylation in a unified approach, as opposed to separate substudies, as done in the literature.[103] Indeed, Zhou et al. simulated the acylation and deacylation steps independently, assuming that the reorganization of the active site's structure is energetically negligible.

The complete reaction profile is depicted in Fig 5. Starting from a structure obtained in previous MD simulations, where ACh is found near the catalytic triad (Point 1 in Fig 5), we identified a transition state structure corresponding to the nucleophilic attack of the oxygen atom from Ser203. The corresponding barrier was found to be less than 10 kcal/mol at the highest QM level (e.g., DLPNO-CCSD(T)). Intermediate 2 resulting from this first step forms a classical tetravalent adduct, benefiting from the stabilization induced by the oxyanion hole (depicted in orange in Fig 5). This initial step is exothermic at the B3LYP–D3/def2–SV(P) level and slightly endothermic at the DLPNO–CCSD(T) level, suggesting that the geometry of the negatively charged adduct is sensitive to active site reorganization. Furthermore, two simultaneous events occur at the transition state TS12: a CO bond is formed, and the proton of the hydroxyl group of Ser203 is transferred to His447.

The next step involves the departure of the choline moiety and the formation of acetylated Ser203. This step is characterized by a smaller barrier (TS23) compared to the first nucleophilic attack, with barriers ranging between 4 and 8 kcal/mol. Simultaneously, the proton on His447 migrates to choline to form the alcohol. The resulting product (Point 3 in Fig 5) is noticeably stable, exhibiting exothermicity between -5 and -6 kcal/mol. Consequently, the initial breakdown of ACh into Ch and acetic acid is characterized by relatively

low barriers, all below 10 kcal/mol, and is exothermic, consistent with the literature.[103]

To proceed with the second part of the reaction (e.g., breaking of acetylated Ser203), a water molecule is essential. This water molecule needs to be positioned to allow for a nucleophilic attack on the carbon of the carbonyl from acetylated Ser203. Consequently, we carefully positioned the closest water molecule (indicated in blue in Fig 5). This re-arrangement revealed a barrier of approximately 20 kcal/mol. Such a high barrier can be attributed to repulsive interactions between the methyl group of acetylated Ser203 and the water molecule.

Intermediate 4 was thus obtained by reorganizing a water molecule in the active site to perform the deacylation step, as described in the previous paragraph. Nucleophilic attack of this water molecule results in a barrier between 0.45 and 1.1 kcal/mol, depending only slightly on the level of calculations. In this step, the formation of the C–O bond is coupled to a proton transfer towards His447, similar to what is obtained during the first step of acylation. The last step is the breaking of the C–OSer203 bond, regenerating Ser203, as characterized by TS56. In this transition state, the proton coming from water and localized on His447 jumps back to the oxygen of Ser203 to restore its activity. This last barrier was found to be between 7.59 and 9.54 kcal/mol.

In summary, no barriers in acylation and deacylation were found higher than 10 kcal/mol. However, a critical barrier was identified as the water migration within the active site, around 20 kcal/mol. The high barrier observed in our simulations allows us to emphasize the importance of treating both acylation and deacylation as a unified computation in our model, rather than conducting them as separate studies.

Step 3: Choline departure through different paths

After ACh undergoes cleavage into Ch and acetate, the release of these products from the active site becomes the next crucial step. Fig 6 illustrates the PMFs associated with various possible exit pathways. Besides the main channel and backdoor pathways discussed earlier,

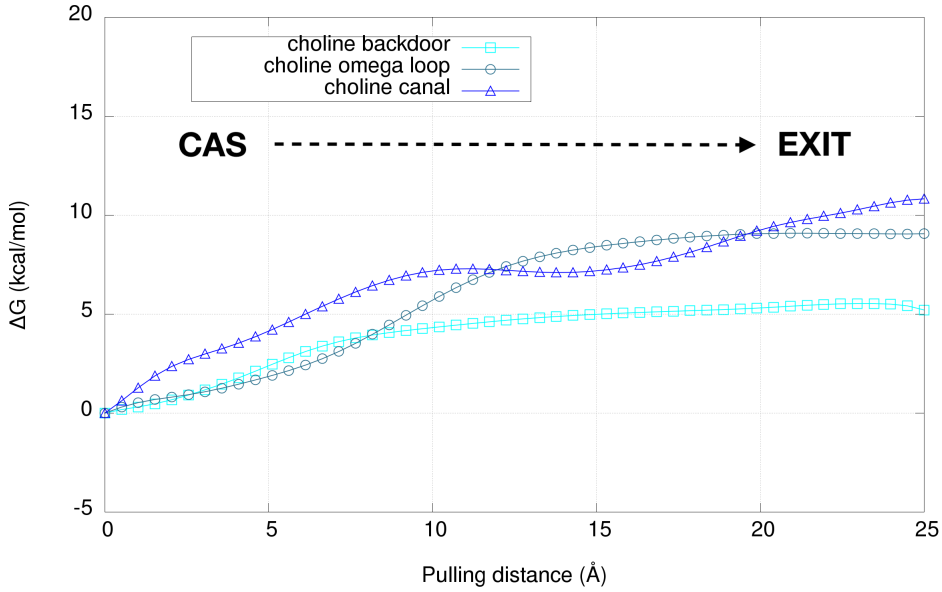

Figure 6: PMF of the release of choline out of the active site through different ways. B: Non–covalent interactions between the protein, the ligand and the water are plotted as a function of simulation time. C: Sum of the cation–π interactions between the ligand and the protein as a function of simulation time.

we retrospectively introduced a third pathway involving Ch exiting through the omega loop. This addition was motivated by intriguing observations from our sets of SMD trajectories concerning the Ch exit. Surprisingly, a subset of these trajectories (see Table T1 and T2 in section 4 of SI) revealed a vacuum–like effect in the omega loop just before Ch was expelled, altering its final exit pathway. Therefore, we extracted these trajectories and recomputed the two distinct PMFs for Ch exiting through the backdoor and the omega loop.

The PMFs for Ch exiting through the main channel (blue curve in Fig 6) and the omega loop (gray curve in Fig 6) exhibit considerable similarity, while the backdoor pathway (cyan curve in Fig 6) presents the most energetically favorable route, with a free energy difference of 5 kcal/mol. This corresponds to differences of 4 and 6 kcal/mol compared to the main channel and omega loop, respectively. The preference for the backdoor route can be first explained by the reduced hydrogen bonding interactions between Ch and AChE during its exit through the backdoor, as well as weaker cation–π interactions (see Fig 7). These factors suggest that Ch encounters fewer energetic penalties when exiting through this pathway.

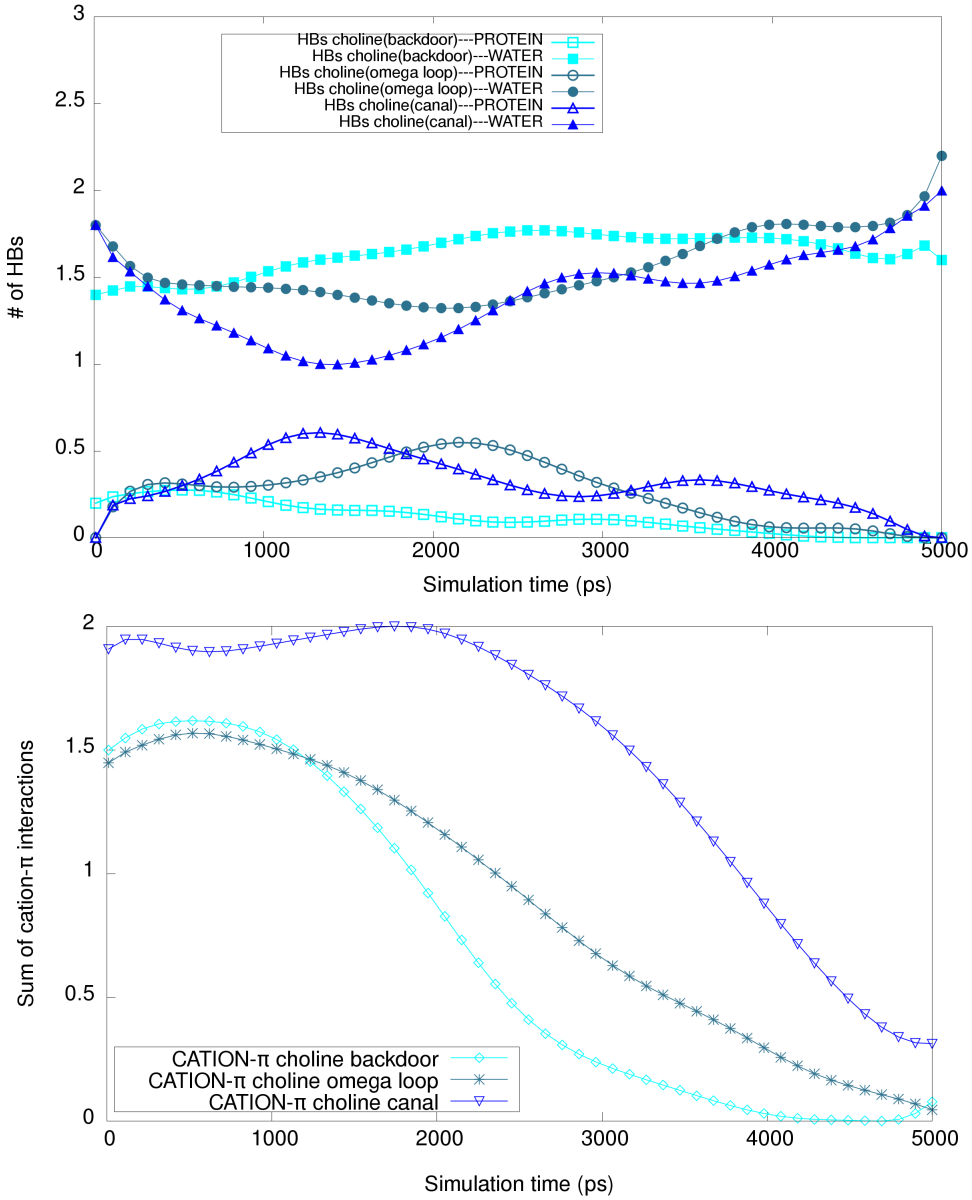

Figure 7: Upper: Hydrogen bonding interactions between the protein, the ligand and the water, plotted as a function of simulation time. Below: Sum of the cation–π interactions between the ligand and the protein as a function of simulation time.

Interestingly, we observed similar hydrogen bonding patterns between Ch and the aromatic residues present in the AChE gorge during the exit of Ch, similar to ACh entrance (see Fig 3), further supporting the consistency of our simulations. Besides, interactions between Trp86 and Ch were noticed (see Fig S5/S6/S7 in section 4 of SI) when Ch does not exit through the main channel, highlighting the role played by the omega loop. As for ACh, we measured the variation of water molecules along the different exit pathways during the simulations and assessed the changes in solvent–accessible surface area, as shown in Figs S3 and S4 in SI. These observations confirm our previous findings, emphasizing Ch's preference for the backdoor exit over the main channel and omega loop.

Importantly, the preference of Ch for the backdoor exit is not a novel observation and has been previously highlighted by Sussman et al.[104] In their work, based on several dozen MD simulations, they reported a 65% probability of Ch exiting through the backdoor. In contrast, our PMFs indicate a 100% selectivity for the backdoor exit compared to the CAS/PAS transition in Fig 6. Although this difference does not align with the results of Sussman et al., it can be attributed to the small free energy difference (2.5 kcal/mol), which falls within the uncertainty range established during the validation of our simulation parameters (e.g., 2 kcal/mol). While thus not directly quantitatively comparable to Sussman et al.'s work, our results nevertheless emphasize the clear preference of Ch for the backdoor exit. Furthermore, the low free energy barrier (e.g., 5 kcal/mol) compared to all previously measured barriers (including steps 1 and 2) suggests that Ch diffusion through the various exit pathways is not the rate–limiting step of the AChE catalysis process as a whole.

Discussion

Through our ensemble of simulations, we assessed the energetic barriers associated with each step of the ACh reaction with AChE. From ACh entry to Ch and acetate exit, no step hindering the reaction progress was observed, supporting experimental findings that AChE exhibits catalytic activity close to the diffusion–limited regime. The rate–limiting step of

the process was identified as the migration of a water molecule facilitating the transition between the acylation and deacylation steps during ACh cleavage by AChE (see step 2 in the Results section). With a transition state barrier of 20 kcal/mol, this step is significantly the most endothermic, suggesting that water molecules in the vicinity of Ser203 may be highly polarized.

a) b)

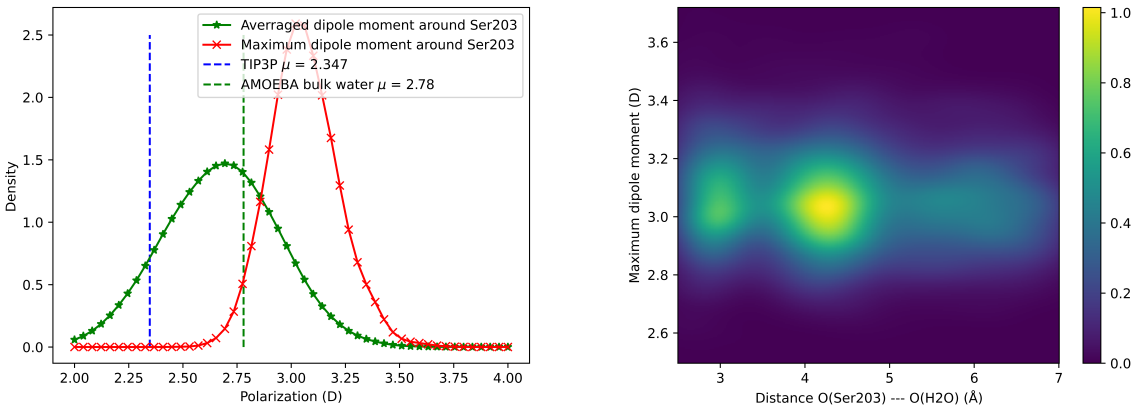

Figure 8: a) Representation of the dipoles distribution in the active site (green curve) and the maximum dipole moment measured in a vicinity of 7 Å of Ser203. b) 2D representation of the distribution of the maximum dipole moment as a function of the distance between the Ser203 and the corresponded water molecule.

To verify our hypothesis, we performed an extensive polarizable MD simulation and analyzed the dipole moments of water molecules in the vicinity of Ser203 (up to 7 from the oxygen of Ser203). The simulation were carried out on the AChE+ACh system (see Fig 2A) for 100 ns using the Tinker–HP software[99] with GPU acceleration[93] and the AMOEBA polarizable force field.[96] The system was fully converted to fit with AMOEBA. Further details on the dynamics setup and the parameterization of ACh for AMOEBA can be found in the Methodological section and SI.

Fig 8a) illustrates the averaged dipole moment of water molecules near Ser203 throughout the full dynamics (green curve). Notably, these water molecules exhibit a lower polarization (0.1 D) compared to the bulk water AMOEBA dipole (2.78 D). These results are consistent with prior studies conducted by our research group,[105,106] confirming the reliability and

validity of our simulations.

However, Fig 8a) also reveals the presence of a highly polarized water molecule around Ser203 during the dynamics (red curve). The average dipole moment increases from 2.69 to 3.10 D, indicating the presence of at least one overpolarized water molecule in the vicinity of Ser203. This polarized water molecule is mainly localized between 3 and 4.5 Å from Ser203, forming two prominent basins in Fig 8b). Interestingly, these basins correspond to the area where Driant et al. previously identified the stabilization of a negatively charged residue at 4.4 Å from Ser203.[27] Thus, our findings support the potential presence of a strongly polarized water molecule in this region, which may explain the high free energy barrier observed during the acylation/deacylation transition.

Conclusions

Through this study, we provide a pipeline aimaing at reconstructing the entire dynamic and reactive profile encompassing all the steps involved in the reactivity of AChE. We used MD and QM/MM approaches to simulate the entire process, ranging from the substrate's entry to its departure as choline and acetate. Our ensemble of simulations revealed first a significant affinity between ACh and its natural enzyme, indicating a strong binding interaction.

Surprisingly, the rate–limiting step in the catalytic cyle of AChE was not attributed neither to the dynamics of the ligands nor the cleavage of ACh into ACh and Ch, but rather to a water reorganization process occuring between the acylation and deacylation reactions. When simulating acylation and deacylation separately, no significant barriers were observed. However, when considering both processes together, a substantial 20 kcal/mol barrier was measured, surpassing all other barriers encountered throughout the entire reaction mechanism (e.g., maximum of 10 kcal/mol). The occurrence of strong water molecule polarization near Ser203 was verified by conducting a long polarizable MD simulation to ascertain the behavior of water molecule dipoles in the vicinity of Ser203. With a maximum dipole moment

estimated at 3.10 D, we can claim that our simulations provide evidence for the significance of accurately treating water molecules when conducting such studies.

Additionally, and although not new, we further confirmed the preference of Ch to exit through the backdoor instead of the main channel. This observation aligns with the findings of Sussman et al., underscoring AChE's ability to facilitate product expulsion via an alternate pathway. By doing so, AChE might enhance its catalytic activity, circumventing any steric clashes that may arise when a new ACh molecule enters the active site while the previous ACh and acetate are yet to be expelled.

Overall, our comprehensive model, elucidating the crucial role of water molecules and their behavior in the active site of AChE, provides fruitful insights into the mechanism governing the complete reactive profile of AChE. We hope that this approach will aid in addressing challenges associated with analogous enzymes in future studies, opening the way for deeper understanding and potential therapeutic applications.

Supporting Information Available

A Supporting Information is available with this draft, containing the following elements:

- Scheme S1: Representation of the Huperzine–A (HUPA) structure.
- Figure S1: Representation of the 30 SMD trajectories for the system AChE+HUPA. The PMF obtained through the Jarzynski equation is depicted with the black bold line.
- Figure S2: Contribution of each residues in the cation–π interactions for the AChE + ACh system.
- Figure S3: Representation of the Solvent Accessible Surface Area (SASA) for each system, computed as a function of simulation time using the VMD software.

- Figure S4: Evolution of the number of water molecules in the gorge as a function of simulation time.
- Table T1: List of the 30 independant SMD trajectories performed on the choline when the SMD vector points out along the main channel.
- Table T2: List of the 30 independant SMD trajectories performed on the choline when the SMD vector points out towards the backdoor.
- Figure S5: Contribution of each residues in the cation–π interactions for the AChE + Ch system with Ch exiting through the main channel.
- Figure S6: Contribution of each residues in the cation–π interactions for the AChE + Ch system with Ch exiting through the backdoor.
- Figure S7: Contribution of each residues in the cation–π interactions for the AChE + Ch system with Ch exiting through the Ω loop.
- Table T3: Energetics values for the various intermediates at the B3LYP–D3/def2–SV(P):CHARMM22 level.
- Table T4: Energetics values for the various intermediates at the B3LYP–D3/def2–TZVPP:CHARMM22//B3LYP–D3/def2–SV(P):CHARMM22 level.
- Table T5: Energetics values for the various intermediates at the DLPNO–CCSD(T)/def2–TZVPP:CHARMM22//B3LYP–D3/def2–SV(P):CHARMM22 level.

Additionnaly, the CHARMM parameters for the ligand HUPA and the AMOEBA parameters for the ligand Ch are provided in sections 1 and 2, respectively. Furthermore, the structures used for each QM/MM computations are also provided in section 5.

Acknowledgement

This work has received funding from the European Research Council (ERC) under the European Union's Horizon 2020 research and innovation program (grant agreement No 810367), project EMC2 (JPP). FC thanks funding from the French state funds managed by the CalSimLab LABEX and the ANR within the Investissements d'Avenir program (reference ANR11-IDEX-0004-02) and support from the Direction Génerale de l'Armement (DGA) Maîtrise NRBC of the French Ministry of Defense. Computations have been performed at GENCI (IDRIS, Orsay, France and TGCC, Bruyères le Chatel) on grant no A0070707671.

Competing interest

The authors declare no competing interests.

List of Figures

List of Tables

References

(1) Marston, S.; Tregear, R.; Rodger, C.; Clarke, M. Coupling between the enzymatic site of myosin and the mechanical output of muscle. *J. Mol. Biol.* **1979**, *128*, 111–126.

(2) Gerlt, J. A. Relationships between enzymatic catalysis and active site structure revealed by applications of site-directed mutagenesis. *Chem. Rev.* **1987**, *87*, 1079–1105.

(3) von Itzstein, M.; Dyason, J. C.; Oliver, S. W.; White, H. F.; Wu, W.-Y.; Kok, G. B.; Pegg, M. S. A study of the active site of influenza virus sialidase: an approach to the rational design of novel anti-influenza drugs. *J. Med. Chem.* **1996**, *39*, 388–391.

(4) Seo, S.; Choi, J.; Park, S.; Ahn, J. Binding affinity prediction for protein–ligand complex using deep attention mechanism based on intermolecular interactions. *BMC bioinform.* **2021**, *22*, 1–15.

(5) Zhao, L.; Zhu, Y.; Wang, J.; Wen, N.; Wang, C.; Cheng, L. A brief review of protein–ligand interaction prediction. *Comput Struct Biotechnol J.* **2022**, *20*, 2831–2838.

(6) Jones, D.; Kim, H.; Zhang, X.; Zemla, A.; Stevenson, G.; Bennett, W. D.; Kirshner, D.; Wong, S. E.; Lightstone, F. C.; Allen, J. E. Improved protein–ligand binding affinity prediction with structure-based deep fusion inference. *J. Chem. Inf. Model.* **2021**, *61*, 1583–1592.

(7) Liu, T.; Lin, Y.; Wen, X.; Jorissen, R. N.; Gilson, M. K. BindingDB: a web-accessible database of experimentally determined protein–ligand binding affinities. *Nucleic Acids Res.* **2007**, *35*, D198–D201.

(8) Gilson, M. K.; Zhou, H.-X. Calculation of protein-ligand binding affinities. *Annu. Rev. Biophys. Biomol. Struct.* **2007**, *36*, 21–42.

(9) Wilker, J. J.; Dmochowski, I. J.; Dawson, J. H.; Winkler, J. R.; Gray, H. B. Substrates

for rapid delivery of electrons and holes to buried active sites in proteins. *Angew. Chem. Int. Ed.* **1999**, *38*, 89–92.

(10) Rossjohn, J.; McKinstry, W. J.; Oakley, A. J.; Verger, D.; Flanagan, J.; Chelvanayagam, G.; Tan, K.-L.; Board, P. G.; Parker, M. W. Human theta class glutathione transferase: the crystal structure reveals a sulfate-binding pocket within a buried active site. *Structure* **1998**, *6*, 309–322.

(11) Kingsley, L. J.; Lill, M. A. Substrate tunnels in enzymes: structure–function relationships and computational methodology. *Proteins.* **2015**, *83*, 599–611.

(12) Urban, P.; Truan, G.; Pompon, D. Access channels to the buried active site control substrate specificity in CYP1A P450 enzymes. *Biochim. Biophys. Acta.* **2015**, *1850*, 696–707.

(13) Wilson, I. B.; Bergmann, F.; Nachmansohn, D. Acetylcholinesterase: X. Mechanism of the catalysis of acylation reactions. *J. Biol. Chem.* **1950**, *186*, 781–790.

(14) Froede, H. C.; Wilson, I. B. Direct determination of acetyl-enzyme intermediate in the acetylcholinesterase-catalyzed hydrolysis of acetylcholine and acetylthiocholine. *J. Biol. Chem.* **1984**, *259*, 11010–11013.

(15) Alberty, R. A.; Hammes, G. G. Application of the theory of diffusion-controlled reactions to enzyme kinetics. *J. Phys. Chem.* **1958**, *62*, 154–159.

(16) Nolte, H.-J.; Rosenberry, T. L.; Neumann, E. Effective charge on acetylcholinesterase active sites determined from the ionic strength dependence of association rate constants with cationic ligands. *Biochemistry.* **1980**, *19*, 3705–3711.

(17) Nachon, F.; Carletti, E.; Ronco, C.; Trovaslet, M.; Nicolet, Y.; Jean, L.; Renard, P.-Y. Crystal structures of human cholinesterases in complex with huprine W and

tacrine: elements of specificity for anti-Alzheimer's drugs targeting acetyl-and butyryl-cholinesterase. *Biochem. J.* **2013**, *453*, 393–399.

(18) Masson, P.; Carletti, E.; Nachon, F. Structure, activities and biomedical applications of human butyrylcholinesterase. *Protein Pept. Lett.* **2009**, *16*, 1215–1224.

(19) Patočka, J.; Kuča, K.; Jun, D. Acetylcholinesterase and butyrylcholinesterase–important enzymes of human body. *Acta Med.* **2004**, *47*, 215–228.

(20) Cheung, J.; Rudolph, M. J.; Burshteyn, F.; Cassidy, M. S.; Gary, E. N.; Love, J.; Franklin, M. C.; Height, J. J. Structures of human acetylcholinesterase in complex with pharmacologically important ligands. *J. Med. Chem.* **2012**, *55*, 10282–10286.

(21) Lazarevic-Pasti, T.; Leskovac, A.; Momic, T.; Petrovic, S.; Vasic, V. Modulators of acetylcholinesterase activity: From Alzheimer's disease to anti-cancer drugs. *Curr. Med. Chem.* **2017**, *24*, 3283–3309.

(22) Pohanka, M.; Hrabinova, M.; Kuca, K.; Simonato, J.-P. Assessment of acetylcholinesterase activity using indoxylacetate and comparison with the standard Ellman's method. *Int. J. Mol. Sci.* **2011**, *12*, 2631–2640.

(23) Day, K. E.; Scott, I. M. Use of acetylcholinesterase activity to detect sublethal toxicity in stream invertebrates exposed to low concentrations of organophosphate insecticides. *Aquat. Toxicol.* **1990**, *18*, 101–113.

(24) Nicolet, Y.; Lockridge, O.; Masson, P.; Fontecilla-Camps, J. C.; Nachon, F. Crystal structure of human butyrylcholinesterase and of its complexes with substrate and products. *J. Biol. Chem.* **2003**, *278*, 41141–41147.

(25) Mercey, G.; Verdelet, T.; Renou, J.; Kliachyna, M.; Baati, R.; Nachon, F.; Jean, L.; Renard, P.-Y. Reactivators of acetylcholinesterase inhibited by organophosphorus nerve agents. *Acc. Chem. Res.* **2012**, *45*, 756–766.

(26) Kwasnieski, O.; Verdier, L.; Malacria, M.; Derat, E. Fixation of the two tabun isomers in acetylcholinesterase: a QM/MM study. *J. Phys. Chem. B.* **2009**, *113*, 10001–10007.

(27) Driant, T.; Nachon, F.; Ollivier, C.; Renard, P.-Y.; Derat, E. On the influence of the protonation states of active site residues on AChE reactivation: a QM/MM approach. *ChemBioChem* **2017**, *18*, 666–675.

(28) Wilson, I. B.; Quan, C. Acetylcholinesterase studies on molecular complementariness. *Arch. Biochem. Biophys.* **1958**, *73*, 131–143.

(29) Mooser, G.; Sigman, D. S. Ligand binding properties of acetylcholinesterase determined with fluorescent probes. *Biochem* **1974**, *13*, 2299–2307.

(30) Ordentlich, A.; Barak, D.; Kronman, C.; Flashner, Y.; Leitner, M.; Segall, Y.; Ariel, N.; Cohen, S.; Velan, B.; Shafferman, A. Dissection of the human acetylcholinesterase active center determinants of substrate specificity. Identification of residues constituting the anionic site, the hydrophobic site, and the acyl pocket. *J. Biol. Chem.* **1993**, *268*, 17083–17095.

(31) Winkler, F.; d'Arcy, A.; Hunziker, W. Structure of human pancreatic lipase. *Nature* **1990**, *343*, 771–774.

(32) Ordentlich, A.; Barak, D.; Kronman, C.; Ariel, N.; Segall, Y.; Velan, B.; Shafferman, A. Functional characteristics of the oxyanion hole in human acetylcholinesterase. *J. Biol. Chem.* **1998**, *273*, 19509–19517.

(33) Ripoll, D. R.; Faerman, C. H.; Axelsen, P. H.; Silman, I.; Sussman, J. L. An electrostatic mechanism for substrate guidance down the aromatic gorge of acetylcholinesterase. *Proc. Nat. Ac. Sci.* **1993**, *90*, 5128–5132.

(34) Shi, J.; Tai, K.; McCammon, J. A.; Taylor, P.; Johnson, D. A. Nanosecond dynamics

of the mouse acetylcholinesterase Cys69–Cys96 omega loop. *J. Biol. Chem.* **2003**, *278*, 30905–30911.

(35) Kumawat, A.; Raheem, S.; Ali, F.; Dar, T. A.; Chakrabarty, S.; Rizvi, M. A. Organoselenium compounds as acetylcholinesterase inhibitors: Evidence and mechanism of mixed inhibition. *J. Phys. Chem. B.* **2021**, *125*, 1531–1541.

(36) Cheng, S.; Song, W.; Yuan, X.; Xu, Y. Gorge motions of acetylcholinesterase revealed by microsecond molecular dynamics simulations. *Sci. Rep.* **2017**, *7*, 1–12.

(37) Shen, T.; Tai, K.; Henchman, R. H.; McCammon, J. A. Molecular dynamics of acetylcholinesterase. *Acc. Chem. Res.* **2002**, *35*, 332–340.

(38) Tara, S.; Helms, V.; Straatsma, T.; McCammon, J. A. Molecular dynamics of mouse acetylcholinesterase complexed with huperzine A. *Biopolymers.* **1999**, *50*, 347–359.

(39) Tai, K.; Shen, T.; Börjesson, U.; Philippopoulos, M.; McCammon, J. A. Analysis of a 10-ns molecular dynamics simulation of mouse acetylcholinesterase. *Biophys. J.* **2001**, *81*, 715–724.

(40) Bui, J. M.; McCammon, J. A. Acetylcholinesterase: pivotal roles of its long omega loop (Cys69-Cys96) in regulating substrate binding. *Chem. Biol. Interact.* **2005**, *157*, 357–359.

(41) Bergmann, F.; Wilson, I. B.; Nachmansohn, D. The inhibitory effect of stilbamidine, curare and related compounds and its relationship to the active groups of acetylcholine esterase. Action of stilbamidine upon nerve impulse conduction. *Biochim. Biophys. Acta.* **1950**, *6*, 217–224.

(42) Cavalli, A.; Bottegoni, G.; Raco, C.; De Vivo, M.; Recanatini, M. A computational study of the binding of propidium to the peripheral anionic site of human acetylcholinesterase. *J. Med. Chem.* **2004**, *47*, 3991–3999.

(43) Branduardi, D.; Gervasio, F. L.; Cavalli, A.; Recanatini, M.; Parrinello, M. The role of the peripheral anionic site and cation- π interactions in the ligand penetration of the human AChE gorge. *J. Am. Chem. Soc.* **2005**, *127*, 9147–9155.

(44) Liang, J.-Y.; Lipscomb, W. N. Binding of substrate CO2 to the active site of human carbonic anhydrase II: a molecular dynamics study. *Proc. Nat. Ac. Sci.* **1990**, *87*, 3675–3679.

(45) Kua, J.; Zhang, Y.; McCammon, J. A. Studying enzyme binding specificity in acetylcholinesterase using a combined molecular dynamics and multiple docking approach. *J. Am. Chem. Soc.* **2002**, *124*, 8260–8267.

(46) Xu, Y.; Shen, J.; Luo, X.; Silman, I.; Sussman, J. L.; Chen, K.; Jiang, H. How does huperzine A enter and leave the binding gorge of acetylcholinesterase? Steered molecular dynamics simulations. *J. Am. Chem. Soc.* **2003**, *125*, 11340–11349.

(47) Khelashvili, G.; Grossfield, A.; Feller, S. E.; Pitman, M. C.; Weinstein, H. Structural and dynamic effects of cholesterol at preferred sites of interaction with rhodopsin identified from microsecond length molecular dynamics simulations. *Proteins.* **2009**, *76*, 403–417.

(48) Bernardi, R. C.; Melo, M. C.; Schulten, K. Enhanced sampling techniques in molecular dynamics simulations of biological systems. *Biochim. Biophys. Acta.* **2015**, *1850*, 872–877.

(49) Yang, Y. I.; Shao, Q.; Zhang, J.; Yang, L.; Gao, Y. Q. Enhanced sampling in molecular dynamics. *J. Chem. Phys.* **2019**, *151*.

(50) Rydzewski, J.; Nowak, W. Ligand diffusion in proteins via enhanced sampling in molecular dynamics. *Phys. Life Rev.* **2017**, *22*, 58–74.

(51) Isralewitz, B.; Gao, M.; Schulten, K. Steered molecular dynamics and mechanical functions of proteins. *Curr. Opin. Struc. Biol.* **2001**, *11*, 224–230.

(52) Izrailev, S.; Stepaniants, S.; Balsera, M.; Oono, Y.; Schulten, K. Molecular dynamics study of unbinding of the avidin-biotin complex. *Biophys. J.* **1997**, *72*, 1568–1581.

(53) Liu, X.; Xu, Y.; Wang, X.; Barrantes, F. J.; Jiang, H. Unbinding of nicotine from the acetylcholine binding protein: steered molecular dynamics simulations. *J. Phys. Chem. B.* **2008**, *112*, 4087–4093.

(54) Zhang, J.-L.; Zheng, Q.-C.; Li, Z.-Q.; Zhang, H.-X. Molecular dynamics simulations suggest ligand's binding to nicotinamidase/pyrazinamidase. *PLoS One.* **2012**, *7*, e39546.

(55) Lüdemann, S. K.; Lounnas, V.; Wade, R. C. How do substrates enter and products exit the buried active site of cytochrome P450cam? 1. Random expulsion molecular dynamics investigation of ligand access channels and mechanisms. *J. Mol. Biol.* **2000**, *303*, 797–811.

(56) Yu, X.; Cojocaru, V.; Wade, R. C. Conformational diversity and ligand tunnels of mammalian cytochrome P 450s. *Biotechnol. Appl. Biochem.* **2013**, *60*, 134–145.

(57) Park, S.; Khalili-Araghi, F.; Tajkhorshid, E.; Schulten, K. Free energy calculation from steered molecular dynamics simulations using Jarzynski's equality. *J. Chem. Phys.* **2003**, *119*, 3559–3566.

(58) Park, S.; Schulten, K. Calculating potentials of mean force from steered molecular dynamics simulations. *J. Chem. Phys.* **2004**, *120*, 5946–5961.

(59) Célerse, F.; Lagardère, L.; Derat, E.; Piquemal, J.-P. Massively parallel implementation of Steered Molecular Dynamics in Tinker-HP: comparisons of polarizable and

non-polarizable simulations of realistic systems. *J. Chem. Theory. Comput.* **2019**, *15*, 3694–3709.

(60) Ghosh, S.; Jana, K.; Ganguly, B. Revealing the mechanistic pathway of cholinergic inhibition of Alzheimer's disease by donepezil: a metadynamics simulation study. *Phys. Chem. Chem. Phys.* **2019**, *21*, 13578–13589.

(61) Niu, C.; Xu, Y.; Xu, Y.; Luo, X.; Duan, W.; Silman, I.; Sussman, J. L.; Zhu, W.; Chen, K.; Shen, J., et al. Dynamic mechanism of E2020 binding to acetylcholinesterase: a steered molecular dynamics simulation. *J. Phys. Chem. B.* **2005**, *109*, 23730–23738.

(62) Rydzewski, J.; Jakubowski, R.; Nowak, W.; Grubmuller, H. Kinetics of huperzine A dissociation from acetylcholinesterase via multiple unbinding pathways. *J. Chem. Theory. Comput.* **2018**, *14*, 2843–2851.

(63) Henchman, R. H.; Tai, K.; Shen, T.; McCammon, J. A. Properties of water molecules in the active site gorge of acetylcholinesterase from computer simulation. *Biophys. J.* **2002**, *82*, 2671–2682.

(64) Pathak, A. K.; Bandyopadhyay, T. Protein–drug interactions with effective polarization in polarizable water: oxime unbinding from AChE gorge. *J. Phys. Chem. B.* **2015**, *119*, 14460–14471.

(65) Pathak, A. K.; Bandyopadhyay, T. Unbinding of fluorinated oxime drug from the AChE gorge in polarizable water: A well-tempered metadynamics study. *Phys. Chem. Chem. Phys.* **2017**, *19*, 5560–5569.

(66) Pathak, A. K.; Bandyopadhyay, T. Dynamic mechanism of a fluorinated oxime reactivator unbinding from AChE gorge in polarizable water. *J. Phys. Chem. B.* **2018**, *122*, 3876–3888.

(67) Ekström, F.; Akfur, C.; Tunemalm, A.-K.; Lundberg, S. Structural changes of phenylalanine 338 and histidine 447 revealed by the crystal structures of tabun-inhibited murine acetylcholinesterase. *Biochemistry.* **2006**, *45*, 74–81.

(68) Carletti, E.; Li, H.; Li, B.; Ekstrom, F.; Nicolet, Y.; Loiodice, M.; Gillon, E.; Froment, M. T.; Lockridge, O.; Schopfer, L. M., et al. Aging of cholinesterases phosphylated by tabun proceeds through O-dealkylation. *J. Am. Chem. Soc.* **2008**, *130*, 16011–16020.

(69) Frisch, A.; Nielson, A.; Holder, A. Gaussview user manual. *Gaussian Inc., Pittsburgh, PA* **2000**, *556*.

(70) Humphrey, W.; Dalke, A.; Schulten, K., et al. VMD: visual molecular dynamics. *J. Mol. Graph.* **1996**, *14*, 33–38.

(71) Phillips, J. C.; Braun, R.; Wang, W.; Gumbart, J.; Tajkhorshid, E.; Villa, E.; Chipot, C.; Skeel, R. D.; Kale, L.; Schulten, K. Scalable molecular dynamics with NAMD. *J. Comput. Chem.* **2005**, *26*, 1781–1802.

(72) Foloppe, N.; A. D. MacKerell, J. All-Atom Empirical Force Field for Nucleic Acids: I. Parameter Optimization Based on Small Molecule and Condensed Phase Macromolecular Target Data. *J. Comput. Chem.* **2000**, *21*, 86–104.

(73) MacKerrell, A. D. J.; et al., All-Atom Empirical Potential for Molecular Modeling and Dynamics Studies of Proteins. *J. Phys. Chem. B* **1998**, *102*, 3586–3616.

(74) MacKerell, A. D. J.; Feig, M.; Brooks, C. L. Extending the Treatment of Backbone Energetics in Protein Force Fields: Limitations of Gas-Phase Quantum Mechanics in Reproducing Protein Conformational Distributions in Molecular Dynamics Simulations. *J. Comput. Chem.* **2004**, *25*, 1400–1415.

(75) Lee, J. et al. CHARMM-GUI Input Generator for NAMD, GROMACS, AMBER, OpenMM, and CHARMM/OpenMM Simulations Using the CHARMM36 Additive Force Field. *J. Chem. Theory. Comput.* **2015**, *1*, 405–413.

(76) Davidchack, R. L.; Handel, R.; Tretyakov, M. Langevin thermostat for rigid body dynamics. *J. Chem. Phys.* **2009**, *130*, 234101.

(77) Darden, T.; York, D.; Pedersen, L. Particle mesh Ewald: An N log (N) method for Ewald sums in large systems. *J. Chem. Phys.* **1993**, *98*, 10089–10092.

(78) Jarzynski, C. Nonequilibrium equality for free energy differences. *Phys. Rev. E.* **1997**, *78*, 2690.

(79) Jarzynski, C. Equilibrium free-energy differences from nonequilibrium measurements: A master-equation approach. *Phys. Rev. E.* **1997**, *56*, 5018.

(80) Pettersen, E. F.; Goddard, T. D.; Huang, C. C.; Couch, G. S.; Greenblatt, D. M.; Meng, E. C.; Ferrin, T. E. UCSF Chimera—a visualization system for exploratory research and analysis. *J. Comp. Chem.* **2004**, *25*, 1605–1612.

(81) Brooks, B. R.; Brooks III, C. L.; Mackerell Jr, A. D.; Nilsson, L.; Petrella, R. J.; Roux, B.; Won, Y.; Archontis, G.; Bartels, C.; Boresch, S., et al. CHARMM: the biomolecular simulation program. *J. Comp. Chem.* **2009**, *30*, 1545–1614.

(82) Søndergaard, C. R.; Olsson, M. H.; Rostkowski, M.; Jensen, J. H. Improved treatment of ligands and coupling effects in empirical calculation and rationalization of p K a values. *J. Chem. Theory. Comput.* **2011**, *7*, 2284–2295.

(83) Olsson, M. H.; Søndergaard, C. R.; Rostkowski, M.; Jensen, J. H. PROPKA3: consistent treatment of internal and surface residues in empirical p K a predictions. *J. Chem. Theory. Comput.* **2011**, *7*, 525–537.

(84) Kastner, J.; Carr, J. M.; Keal, T. W.; Thiel, W.; Wander, A.; Sherwood, P. DL-FIND: an open-source geometry optimizer for atomistic simulations. *J. Phys. Chem. A* **2009**, *113*, 11856–11865.

(85) Furche, F.; Ahlrichs, R.; Hättig, C.; Klopper, W.; Sierka, M.; Weigend, F. Turbomole. *Wiley Interdiscip. Rev. Comput. Mol. Sci.* **2014**, *4*, 91–100.

(86) Becke, A. D. A new mixing of Hartree–Fock and local density-functional theories. *J. Chem. Phys.* **1993**, *98*, 1372–1377.

(87) Grimme, S.; Antony, J.; Ehrlich, S.; Krieg, H. A consistent and accurate ab initio parametrization of density functional dispersion correction (DFT-D) for the 94 elements H-Pu. *J. Chem. Phys.* **2010**, *132*, 154104.

(88) Zheng, J.; Xu, X.; Truhlar, D. G. Minimally augmented Karlsruhe basis sets. *Theor. Chem. Acc.* **2011**, *128*, 295–305.

(89) Todorov, I. T.; Smith, W.; Trachenko, K.; Dove, M. T. DL_POLY_3: new dimensions in molecular dynamics simulations via massive parallelism. *J. Mater. Chem.* **2006**, *16*, 1911–1918.

(90) Lu, Y.; Farrow, M. R.; Fayon, P.; Logsdail, A. J.; Sokol, A. A.; Catlow, C. R. A.; Sherwood, P.; Keal, T. W. Open-source, python-based redevelopment of the ChemShell multiscale QM/MM environment. *J. Chem. Theory. Comput.* **2018**, *15*, 1317–1328.

(91) Neese, F. Software update: the ORCA program system, version 4.0. *Wiley Interdiscip. Rev. Comput. Mol. Sci.* **2018**, *8*, e1327.

(92) Guo, Y.; Riplinger, C.; Becker, U.; Liakos, D. G.; Minenkov, Y.; Cavallo, L.; Neese, F. Communication: An improved linear scaling perturbative triples correction for the domain based local pair-natural orbital based singles and doubles coupled cluster method [DLPNO-CCSD (T)]. *J. Chem. Phys.* **2018**, *148*, 011101.

(93) Adjoua, O.; Lagardère, L.; Jolly, L.-H.; Durocher, A.; Very, T.; Dupays, I.; Wang, Z.; Inizan, T. J.; Célerse, F.; Ren, P., et al. Tinker-hp: Accelerating molecular dynamics simulations of large complex systems with advanced point dipole polarizable force fields using gpus and multi-gpu systems. *J. Chem. Theory. Comput.* **2021**, *17*, 2034–2053.

(94) Ren, P.; Ponder, J. W. Polarizable atomic multipole water model for molecular mechanics simulation. *J. Phys. Chem. B.* **2003**, *107*, 5933–5947.

(95) Shi, Y.; Xia, Z.; Zhang, J.; Best, R.; Wu, C.; Ponder, J. W.; Ren, P. Polarizable atomic multipole-based AMOEBA force field for proteins. *J. Chem. Theory. Comput.* **2013**, *9*, 4046–4063.

(96) Zhang, C.; Lu, C.; Jing, Z.; Wu, C.; Piquemal, J.-P.; Ponder, J. W.; Ren, P. AMOEBA polarizable atomic multipole force field for nucleic acids. *J. Chem. Theory. Comput.* **2018**, *14*, 2084–2108.

(97) Rackers, J. A.; Wang, Z.; Lu, C.; Laury, M. L.; Lagardère, L.; Schnieders, M. J.; Piquemal, J.-P.; Ren, P.; Ponder, J. W. Tinker 8: software tools for molecular design. *J. Chem. Theory. Comput.* **2018**, *14*, 5273–5289.

(98) Lagardère, L.; Aviat, F.; Piquemal, J.-P. Pushing the limits of multiple-time-step strategies for polarizable point dipole molecular dynamics. *J. Phys. Chem. Lett.* **2019**, *10*, 2593–2599.

(99) Lagardère, L.; Jolly, L.-H.; Lipparini, F.; Aviat, F.; Stamm, B.; Jing, Z. F.; Harger, M.; Torabifard, H.; Cisneros, G. A.; Schnieders, M. J., et al. Tinker-HP: a massively parallel molecular dynamics package for multiscale simulations of large complex systems with advanced point dipole polarizable force fields. *Chem. Sci.* **2018**, *9*, 956–972.

(100) Bai, F.; Xu, Y.; Chen, J.; Liu, Q.; Gu, J.; Wang, X.; Ma, J.; Li, H.; Onuchic, J. N.; Jiang, H. Free energy landscape for the binding process of Huperzine A to acetylcholinesterase. *Proc. Nat. Ac. Sci.* **2013**, *110*, 4273–4278.

(101) Sussman, J. L.; Harel, M.; Frolow, F.; Oefner, C.; Goldman, A.; Toker, L.; Silman, I. Atomic structure of acetylcholinesterase from Torpedo californica: a prototypic acetylcholine-binding protein. *Science* **1991**, *253*, 872–879.

(102) Changeux, J.-P.; Podleski, T.; Meunier, J.-C. On some structural analogies between acetylcholinesterase and the macromolecular receptor of acetylcholine. *J. Gen. Physiol.* **1969**, *54*, 225–244.

(103) Zhou, Y.; Wang, S.; Zhang, Y. Catalytic reaction mechanism of acetylcholinesterase determined by Born- Oppenheimer ab initio QM/MM molecular dynamics simulations. *J. Phys. Chem. B.* **2010**, *114*, 8817–8825.

(104) Xu, Y.; Colletier, J.-P.; Weik, M.; Qin, G.; Jiang, H.; Silman, I.; Sussman, J. L. Long route or shortcut? A molecular dynamics study of traffic of thiocholine within the active-site gorge of acetylcholinesterase. *Biophys. J.* **2010**, *99*, 4003–4011.

(105) Inizan, T. J.; Célerse, F.; Adjoua, O.; El Ahdab, D.; Jolly, L.-H.; Liu, C.; Ren, P.; Montes, M.; Lagarde, N.; Lagardère, L., et al. High-resolution mining of the SARS-CoV-2 main protease conformational space: supercomputer-driven unsupervised adaptive sampling. *Chem. Sci.* **2021**, *12*, 4889–4907.

(106) El Ahdab, D.; Lagardère, L.; Inizan, T. J.; Célerse, F.; Liu, C.; Adjoua, O.; Jolly, L.-H.; Gresh, N.; Hobaika, Z.; Ren, P., et al. Interfacial Water Many-body Effects Drive Structural Dynamics and Allosteric interactions in SARS-CoV-2 Main Protease Dimerization Interface. *J. Phys. Chem. Lett.* **2021**, *12*, 6218–6226.

Graphical TOC Entry